Supporting Information

Halide-Mixed Dimensional Bridging Enables Thermally Robust Copper-Based Pixelated Scintillators for 3D X-ray Imaging

Lian Wang[a,c], Rubin Wang[a,c], Yaping Chen[a,c], Junxi Chen[b], Chenrui Wang[a], Jiankun Xue[a,c], Hao Lu[a,b,*], Xin Huang[a], Yi Zheng[a], Min Chen[a], Xiaoming Jiang[a], Xieming Xu[a,b,*], Shuaihua Wang[a,b], and Shaofan Wu[a]

[a]Key Laboratory of Optoelectronic Materials Chemistry and Physics, Fujian Institute of Research on the Structure of Matter, Chinese Academy of Sciences, Fuzhou, Fujian 350002, China.

[b]Fujian Science & Technology Innovation Laboratory for Optoelectronic Information of China, Fuzhou, Fujian 350108, China.

[c]University of Chinese Academy of Sciences, Beijing, 100049, China.

*Corresponding authors:

E-mail: xuxieming@fjoel.cn

Experimental Section

Materials: Cesium chloride (CsCl, 99.99%), cesium iodide (CsI, 99.9%), copper(I) iodide (CuI, 99.95%), and N, N-dimethylformamide (DMF, 99.9%) were purchased from Aladdin Company. Ethanol (C_2H_6O, AR), toluene (C_7H_8, 99.7%), hypophosphorous acid (H_3PO_2, 99.7%), isopropanol (C_3H_8O, 99.9%), and cyclohexane (C_6H_{12}, 99.7%) were purchased from Sinopharm Group. All reagents and solvents were used as received without further purification.

Synthesis of Cl⁻-doped copper halide perovskite crystals: copper halide perovskite crystals were synthesized via the anti-solvent method. Based on the optimized $Cs_3Cu_2I_5$ ratio of CsI: CuI = 2.7:2, a gradient synthesis was achieved by progressively replacing CsI with CsCl to adjust the Cl^-/ I^- feed ratio under fixed CuI loading conditions. The specific products are as follows, pure CCI was obtained at a Cl^{-}/ I^{-} molar ratio of 0:5 (without CsCl addition). Intermediate phase products were obtained at Cl^{-}/ I^{-} ratios of 0.5:4.5 and 1.5:3.5. Pure CCCLI was successfully synthesized at a Cl^{-}/ I^{-} molar ratio of 2:3. The synthesis procedure is as follows, raw materials were dissolved in an appropriate amount of DMF to form a precursor solution, with a small amount of H_3PO_2 added to prevent oxidation. The precursor solution was then added to toluene (DMF: C_7H_8 = 1:2) to rapidly reach saturation, causing instantaneous precipitation of a white powder. Wash the powder with cyclohexane three times, centrifuge and dry it, and finally obtain the target product.

Preparation of PDMS Microporous Templates: Take an appropriate amount of PDMS adhesive (A component: B component = 10:1), dispense it onto the microcolumn array mold (fabricated via photolithography), cure by heating at 100°C, then peel off the PDMS to obtain the PDMS microporous template.

Preparation of CCCLI/ PDMS Pixelated Films: First, place the PDMS template in ethanol and sonicate for 30 minutes, then dry in an oven. Subsequently, add CCCLI microcrystalline powder to an appropriate amount of isopropyl alcohol and ball mill for one hour, ultimately yielding a uniformly mixed, fine powder slurry. Next, use a silicone squeegee to apply the powder slurry into the small holes of the PDMS template. After 3-5 passes, gently wipe the surface powder off the film using lint-free paper moistened with ethanol. Finally, dry the film to obtain the pixelated CCCLI/ PDMS scintillation array.

Characterization: XRD data were collected using a Rigaku Miniflex600 diffractometer with a graphite-monochromatized Cu Kα radiation (λ = 1.5418 Å). TGA curve was performed using a Netzsch STA449F3 thermal analyzer at a heating rate of $10°C\cdot min^{-1}$ under a nitrogen atmosphere. The RL data of the collected samples under X-ray irradiation were tested on a photon counting and spectral acquisition device equipped with a (W-target, 5 W) X-ray source. The PL spectra, PLE spectra, and the corresponding decay curves are recorded and collected using an FLS1000 fluorescence spectrometer equipped with an Xe lamp. The temperature-dependent PL spectra were measured by the same fluorescence spectrometer equipped with the cryogenic liquid nitrogen equipment. The temperature-dependent RL spectra were measured by the same fluorescence resonance spectrometer equipped with a (W-target, 5 W) X-ray source and cryogenic liquid nitrogen equipment. TL curves were recorded with an LTTL-3DS model TL 3D spectrometer from 300 to 500 K. The samples were preirradiated with X-ray at a dose of 42.29 $mGy\cdot s^{-1}$ for 10 min at room temperature and then heated from 300 K with a heating rate of 1 $K\cdot s^{-1}$. The light yield measurement was carried out using a photon-counting and spectral acquisition setup equipped with a tungsten-target X-ray source to record the radioluminescence data of the samples and $Bi_4Ge_3O_{12}$ (BGO) under X-ray irradiation. With the X-ray source operating at a voltage of 50 kV and a current of 100 μA, the dose rate at the sample position was 42.29 $mGy\cdot s^{-1}$. A photomultiplier tube (PMT R928) was then used to measure the radiation response amplitudes of the samples and BGO. The absolute light yield was calculated using Equation (1), with the spectra corrected by the wavelength-dependent quantum efficiency curve of the PMT (supplier's calibration data).

Compositional Doping Simulations: The density functional theory calculations were performed using the Vienna ab initio simulation package (VASP), including the effect of core electrons, were described using the projector augmented wave method. A plane-wave energy cutoff of 450 eV and a k-point mesh of 3×3×3 were used in the geometric relaxation. The compositional doping of $Cs_5Cu_3I_{8-x}Cl_x$ was carried out in the single cell and all structures were geometrically relaxed until the total force on each ion was below 0.03 eV $Å^{-1}$.

X-Ray Imaging: X-ray imaging tests were performed using a self-built X-ray imaging system, which includes a MagPro X-ray Source (operated at 50 kV and 100 μA), an imaging object stand, and the scintillation film. The distance from the sample to the X-ray source is 10 cm. The exposure time for each projection was 15s with a gain of ISO 6400. X-ray imaging tests at different temperatures are equipped with heating rings, with the maximum temperature of the heating rings reaching 480 K.

3D X-ray imaging reconstruction: 3D X-ray imaging was conducted using a custom-designed radiographic platform consisting of a Canon 5D4 camera, a motorized 360° rotation stage, an X-ray source, and a dedicated sample holder. Tomographic reconstruction was performed using the 3D Slicer software package. During the imaging process, the angular step size for individual projections was typically set between 1° and 5°, and a minimum rotation range of 180° was required to achieve complete tomographic coverage. The reconstruction procedure relies on accurately extracting the internal structural density distribution from the two-dimensional projections collected at multiple viewing angles. In this study, raw projections were recorded at 5° angular intervals. It should be emphasized that the specimen must rotate precisely about the central axis of the rotation stage to avoid trajectory-related artifacts caused by off-axis motion, which would significantly compromise the reconstruction fidelity.

Figure Section

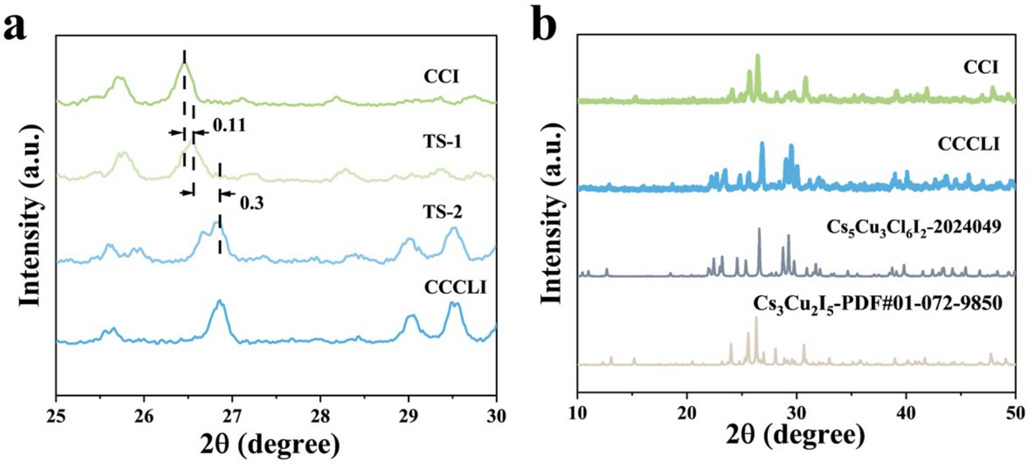

Figure S1. (a) Local magnified XRD patterns of CCI, CCCLI and Cl^- doping TS. (b) XRD patterns of CCI and CCCLI and their corresponding standard PDF cards.

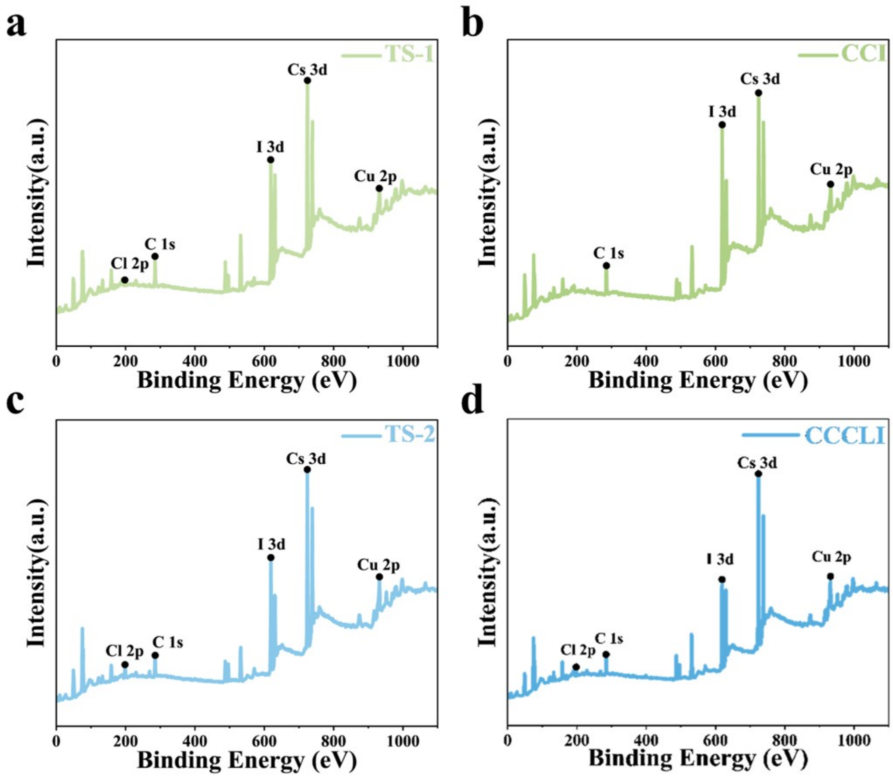

Figure S2. XPS Full Spectrum of CCI, CCCLI and Cl⁻ doping TS.

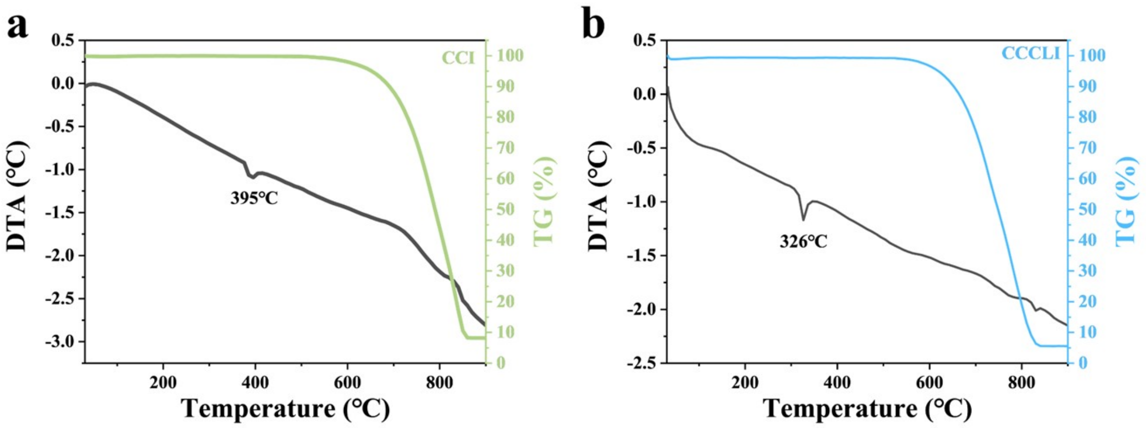

Figure S3. TG-DTA curves of (a) CCI and (b) CCCLI.

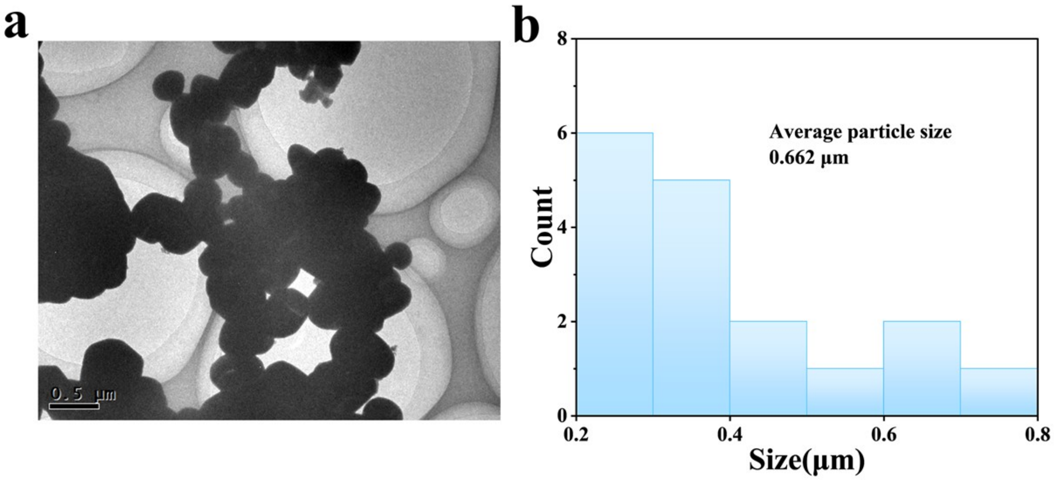

Figure S4. (a) TEM images of CCCLI. (b) Particle size distribution of CCCLI.

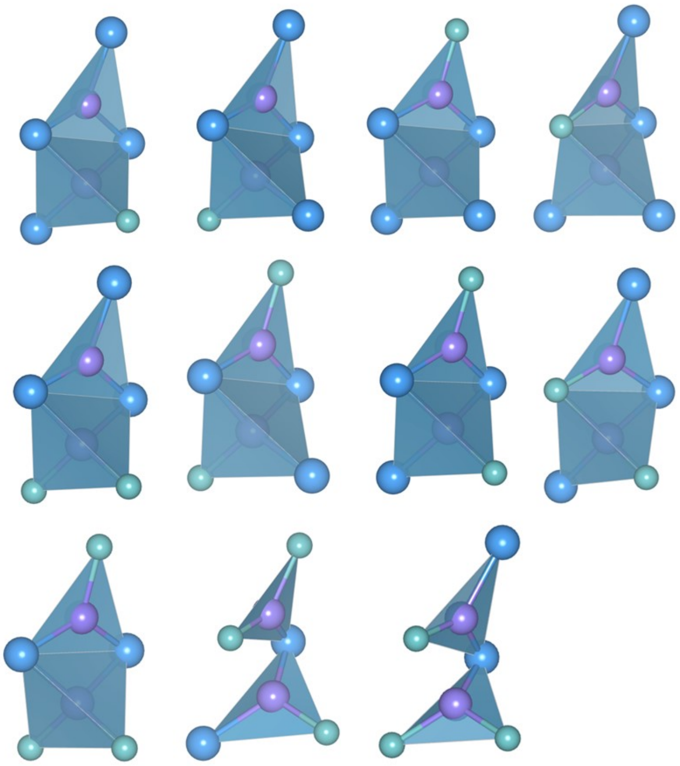

Figure S5. Component Doping Simulation of CCI, CCCLI and Cl⁻ doping TS.

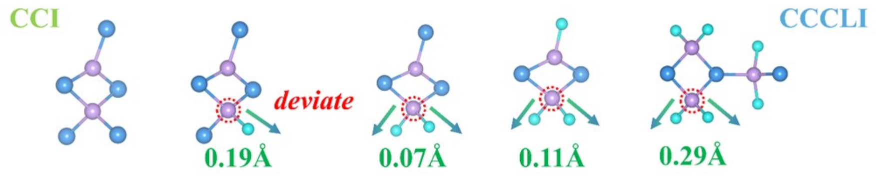

Figure S6. Distance from the central atom to the tetrahedral center of gravity in CCI, CCCLI and Cl⁻ doping TS.

$$D = \frac{1}{n}\sum_{i=1}^{n}\frac{|l_i - l_{av}|}{l_{av}}$$

Here, l_i denotes the distance from the central atom to the ith coordinating atom, and l_{av} represents the average bond length.

$$\lambda = \frac{1}{n}\sum_{i=1}^{n}\left(\frac{l_i}{l_0}\right)^2$$

l_0 is the distance from the center to the vertices of a regular polyhedron of the same volume. λ is the dimensionless quantity that provides a quantitative measure of polyhedral distortion, independent of the polyhedron's effective dimensions.

$$\sigma^2 = = \frac{1}{m-1}\sum_{i=1}^{m}(\phi_i - \phi_0)^2$$

Here, *m* denotes the number of faces in the polyhedron, and ϕ_i represents the i-th bond angle, which is the ideal bond angle of the ϕ_0 regular polyhedron.

Δr is the distance between the tetrahedron's centroid and the Cu atom.

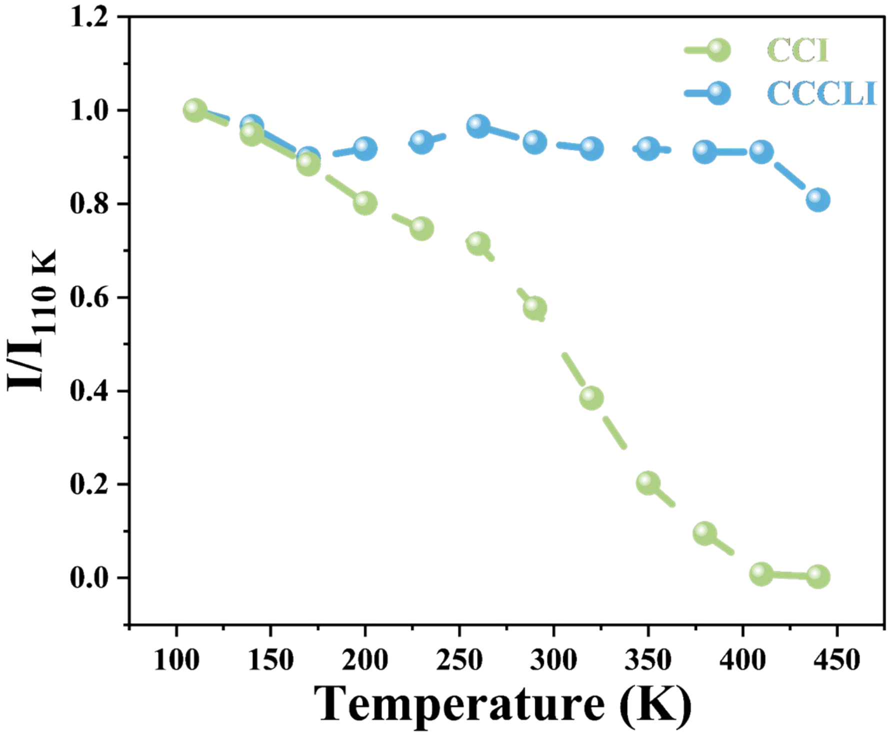

Figure S7. The temperature-dependent luminescence intensity ratio of CCI and CCCLI is I/ I_1 at 110 K.

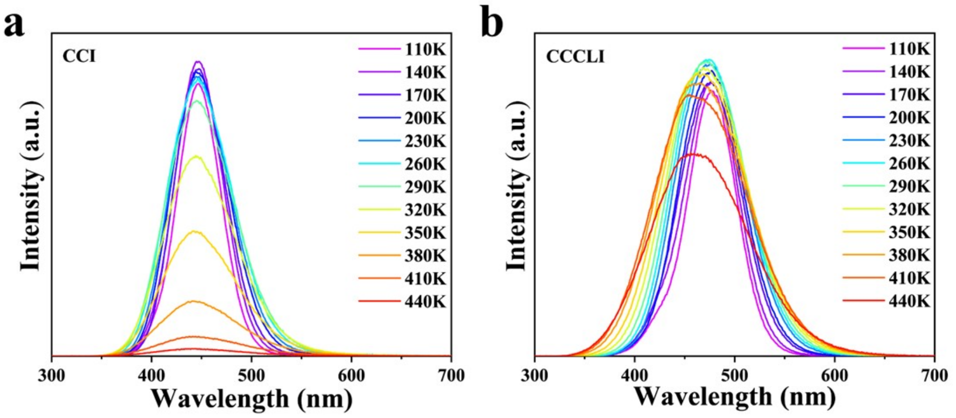

Figure S8. Temperature-dependent fluorescence spectra of (a) CCI and (b) CCCLI.

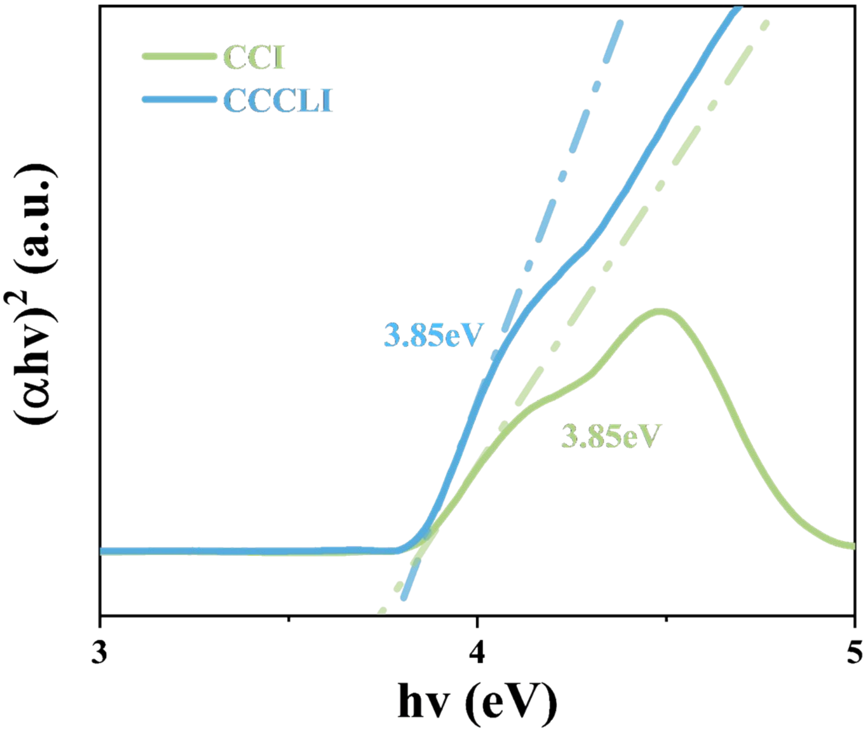

Figure S9. Kubelka-Munk Diagrams and Bandgap Extrapolation for CCI and CCCLI.

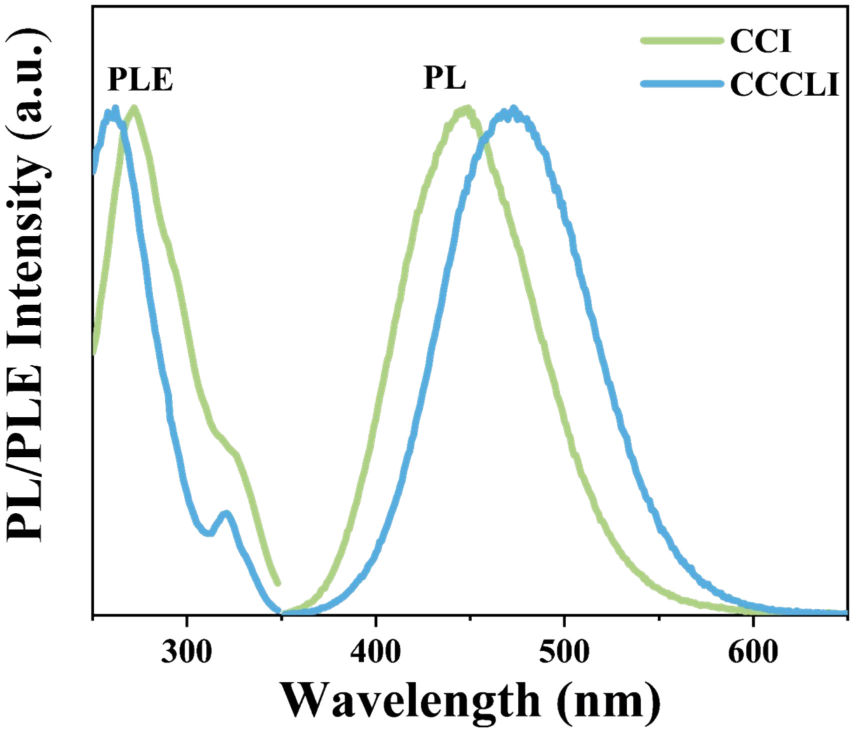

Figure S10. Photoluminescence excitation (PLE) and photoluminescence (PL) spectra of CCI and CCCLI.

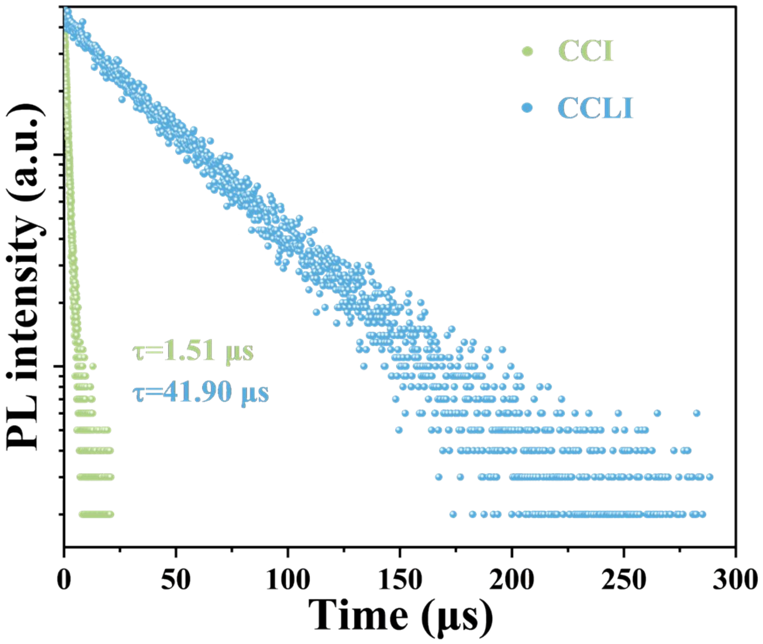

Figure S11. Time-resolved photoluminescence decay curves of CCI (λ_{ex} = 272 nm, λ_{em} = 448 nm, R^2 = 0.99) and CCCLI(λ_{ex} = 262 nm, λ_{em} = 472 nm, R^2 = 0.99).

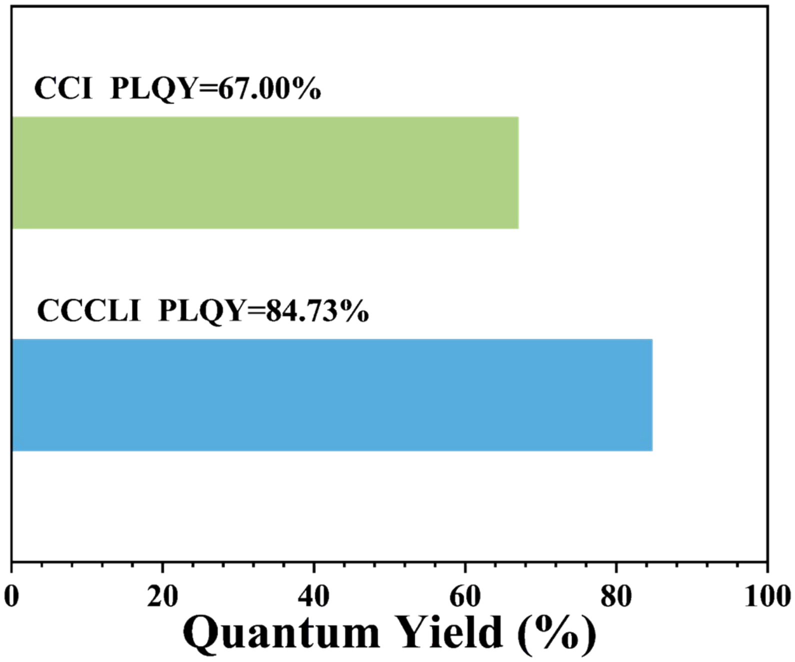

Figure S12. Fluorescence Quantum Yields of CCI and CCCLI.

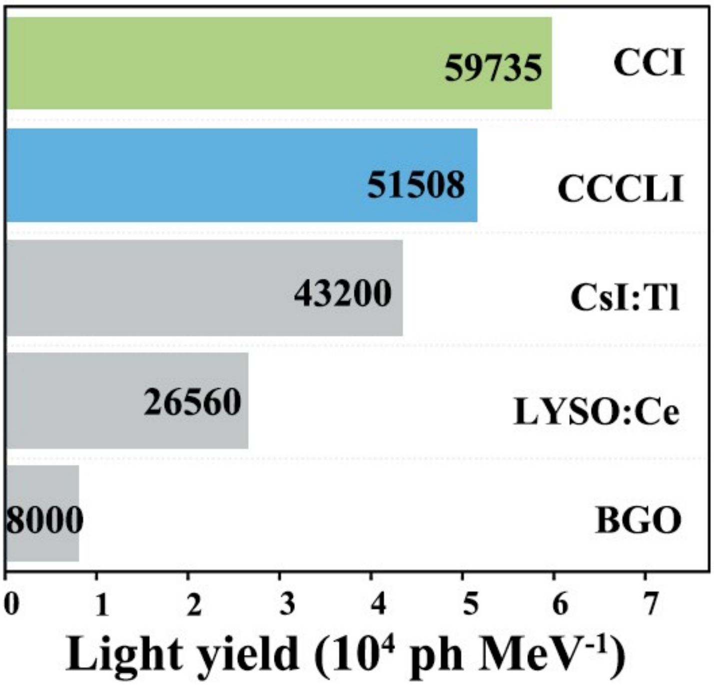

Figure S13. Light yield comparison of CCI, CCCLI, Cs:Tl, LYSO:Ce, and BGO.

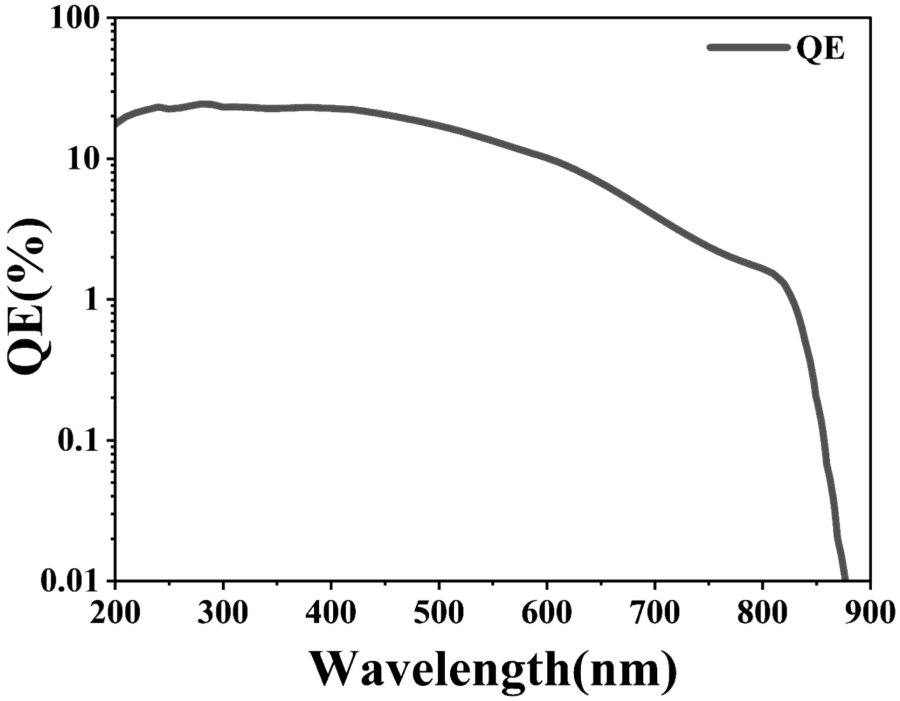

Figure S14. The detection efficiency of the PMT.

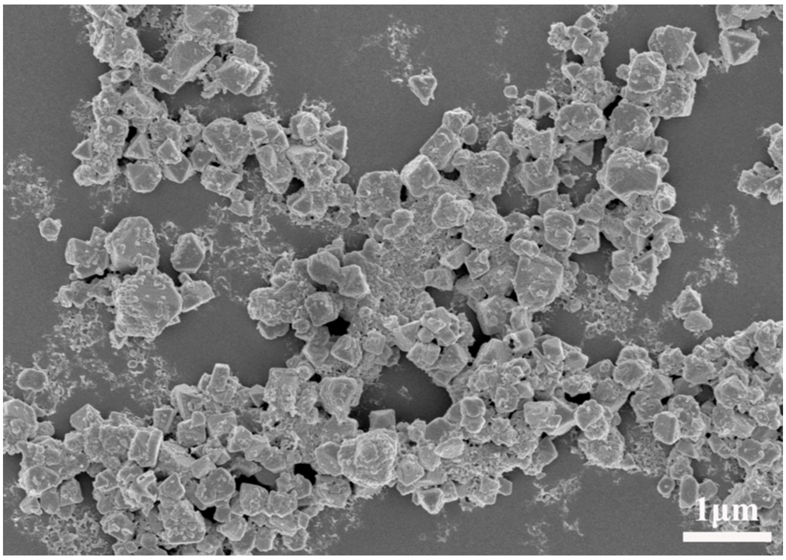

Figure S15. SEM image of ball-milled CCCLI powder.

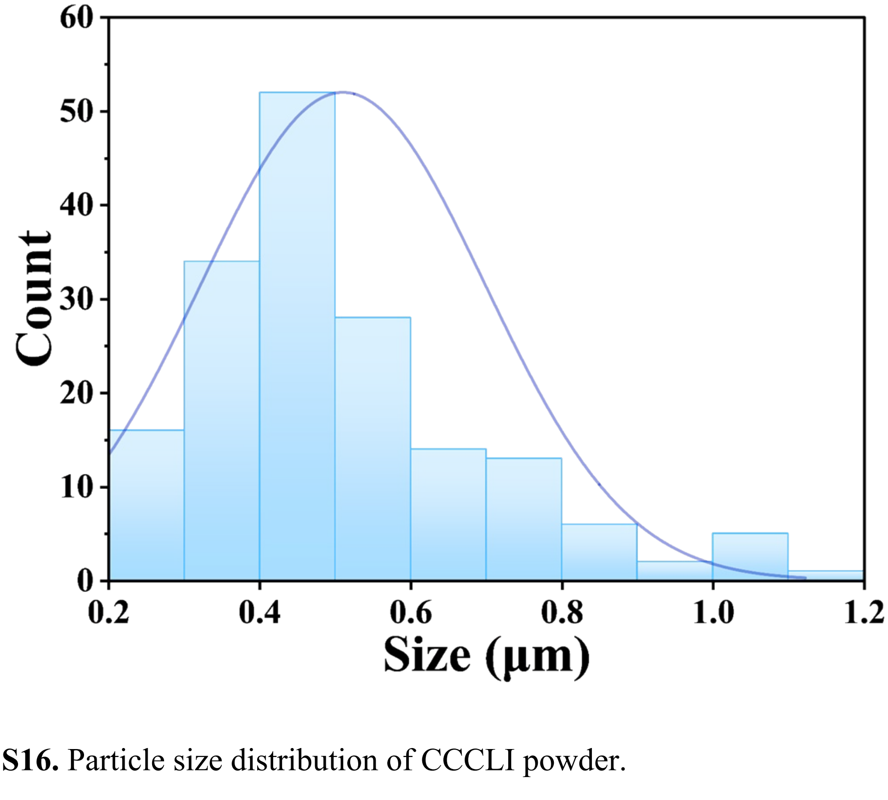

Figure S16. Particle size distribution of CCCLI powder.

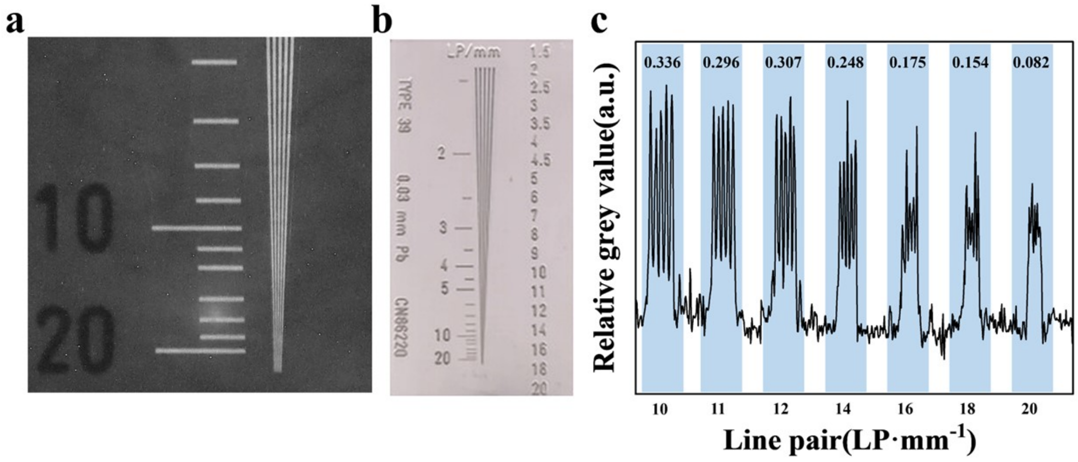

Figure S17. (a) X-ray image of a pixelated scintillation film with 1.7 μm aperture. (b) Standard resolution card. (c)relationship between relative light intensity of the scintillation film and pixels.

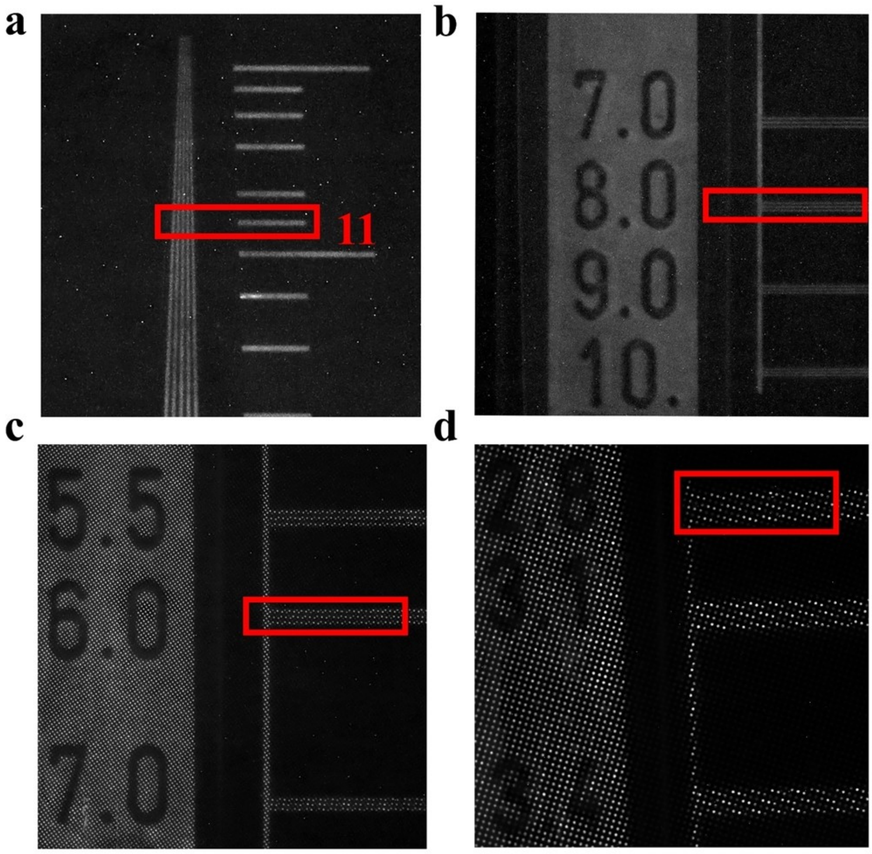

Figure S18. X-ray images of pixelated scintillation films with pore sizes of (a) 10 μm, (b) 20 μm, (c) 50 μm and (d) 100 μm, respectively.

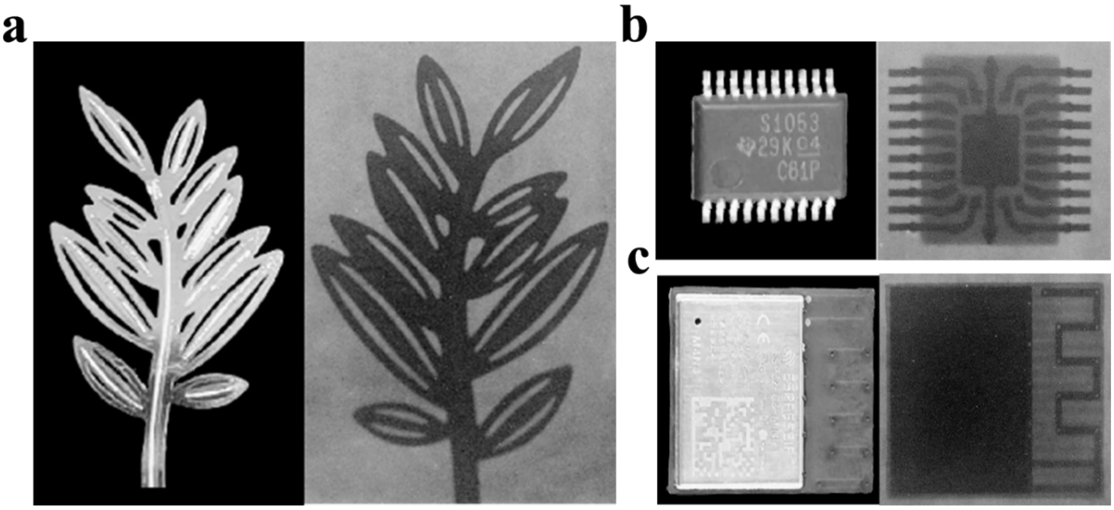

Figure S19. (a) Photographs of the metallic leaf. (b, c) chips and their X-ray images.

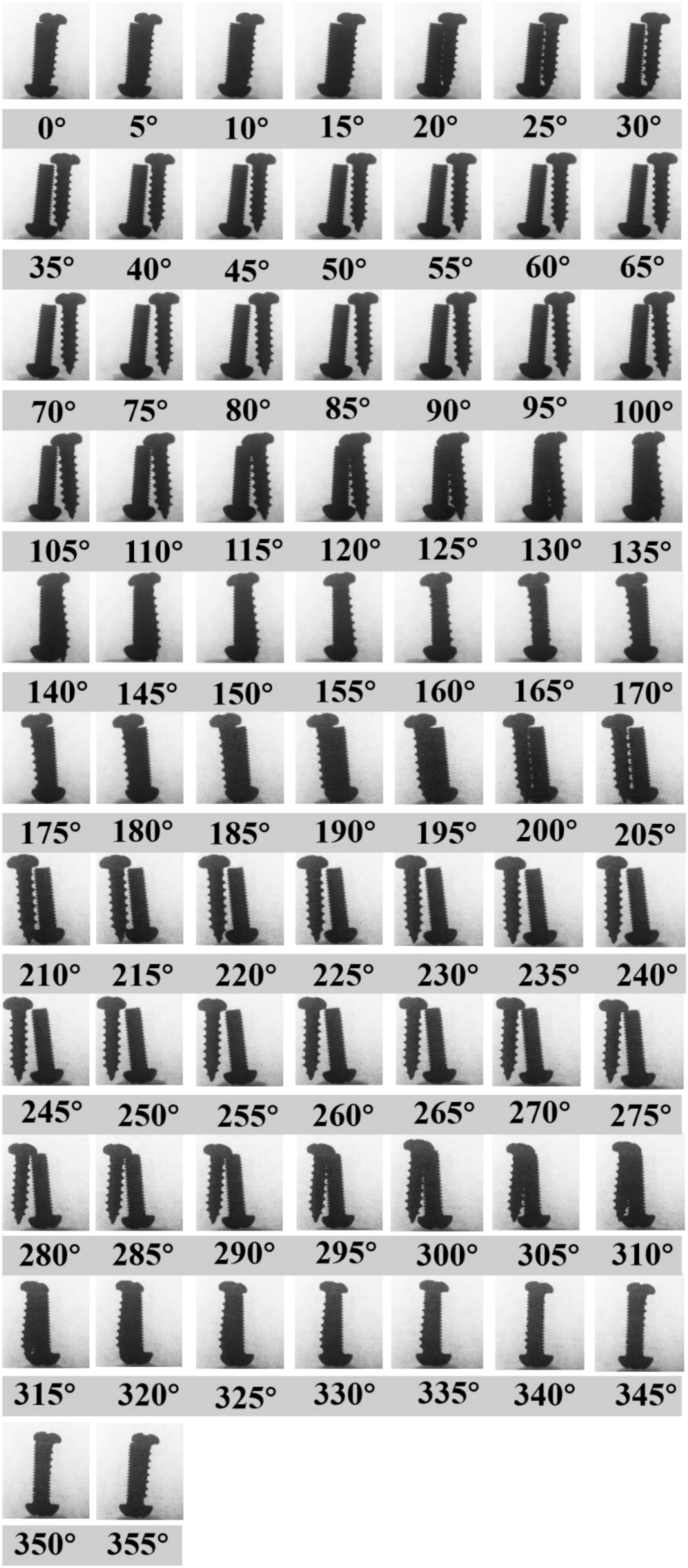

Figure S20. Two-dimensional X-ray images of a screw at different rotation angles.

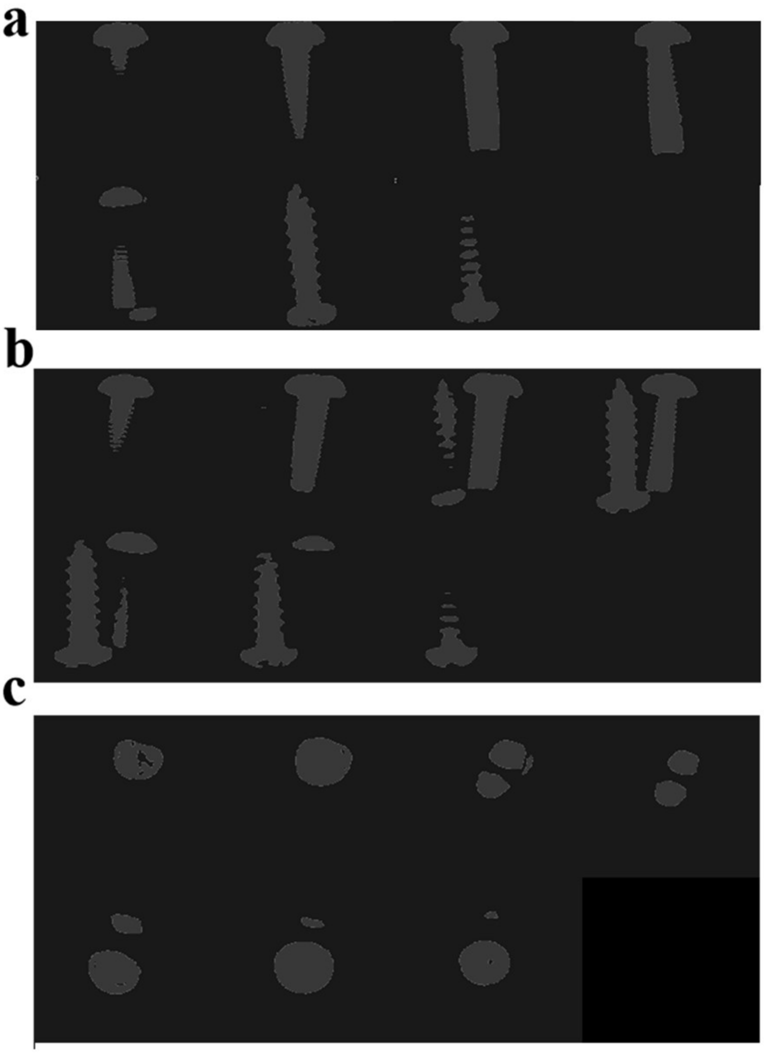

Figure S21. (a) X-axis slices, (b) Y-axis slices, and (c) Z-axis slices of the segmented reconstructed model.

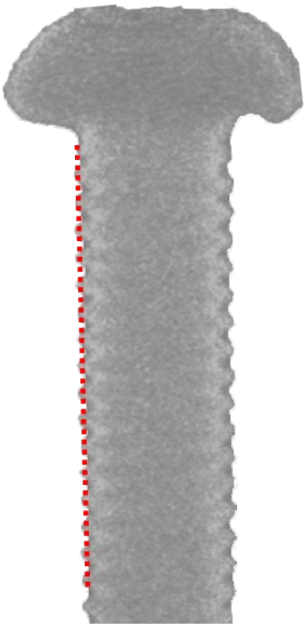

Figure S22. Positioning of the screw contour line in the X-axis slice.

Figure S23. In-situ X-ray imaging of the physical object.

Movie Section

Movie S1. The real-time display of the 3D reconstruction model and tomographic slices with different perspectives.

Table Section

Table S1. Formation energy analysis of CCI, $Cs_3Cu_2I_4Cl_1$, $Cs_3Cu_2I_3Cl_2$, $Cs_3Cu_2I_2Cl_3$, and CCCLI.

Compound	E_{Total} (kJ mol^{-1})	ΔH_f
CCI	-2657.78	-84.15
$Cs_3Cu_2I_4Cl_1$	-2763.67	-108.02
$Cs_3Cu_2I_3Cl_2$	-2858.94	-117.55
$Cs_3Cu_2I_2Cl_3$	-2958.61	-127.51
CCCLI	-4908.69	-132.90

The formation energies are defined as:

$$\Delta H_f \approx [E_{Total} - a \times E(Cs) - b \times E(Cu) - \frac{c}{2}E(I_2) - \frac{d}{2} \times E(Cl_2)]/\mu$$

E_{Total} is the total energy of CCI, $Cs_3Cu_2I_4Cl_1$, $Cs_3Cu_2I_3Cl_2$, $Cs_3Cu_2I_2Cl_3$, and CCCLI; a, b,c and d are the corresponding numbers in the chemical formula; μ is the number of atoms and cations in the unit cell. E(Cs), E(Cu), $E(I_2)$, and $E(Cl_2)$ are energies of the Cs cation, Cu bulk, I_2 and Cl_2 in the 3×3×3 k-mesh, respectively.

Table S2 Comparison of key X-ray scintillation performance metrics of $Cs_5Cu_3Cl_6I_2$ with representative lead-free and commercial scintillators.

Material	Light yield (photons/MeV)	Detection limit	Resolution (lp/mm)	References
$Cs_5Cu_3Cl_6I_2$	51508	8.43 $nGy \cdot s^{-1}$	14	This work
$CsPbBr_3$	26,000	120 $nGy \cdot s^{-1}$	12.5	[1, 2]
$CsMnCl_3$	13,400	470 $\mu Gy \cdot s^{-1}$	4.0	[3]
CsI:TI	65,000	180 $nGy \cdot s^{-1}$	10	[4, 5]
$(BA)_2PbBr_4$	7,900	318.3 $nGy \cdot s^{-1}$	-	[6, 7]
Cs_2HfCl_6	21700	55 $nGy \cdot s^{-1}$	11.2	[8]
Rb_2AgBr_3	25600	19 $nGy \cdot s^{-1}$	10.2	[9]

Table S3 Parameters for PDMS Microporous Templates of Different Specifications.

Template parameters		
aperture(um)	**Pitch(um)**	**depth(um)**
1.7	**1.3**	**3**
10	**10**	**15**
20	**20**	**40**
50	**50**	**50**
100	**100**	**150**

References

[1] W. Chen, M. Zhou, Y. Liu, X. Yu, C. Pi, Z. Yang, H. Zhang, Z. Liu, T. Wang, J. Qiu, S. F. Yu, Y. Yang, X. Xu, *Adv. Funct. Mater.*, 2022, **32**, 2107424.

[2] F. Maddalena, A. Xie, X. Y. Chin, R. Begum, M. E. Witkowski, M. Makowski, B. Mahler, W. Drozdowski, S. V. Springham, R. S. Rawat, N. Mathews, C. Dujardin, M. D. Birowosuto and C. Dang, *J. Phys. Chem. C*, 2021, **125**, 14082.

[3] S. Wang, W. Huang, X. Liu, S. Wang, H. Ye, S. Yu, X. Song, Z. Liu, P. Wang, T. Yang, D. Chu, J. Gou, M. Yuan, L. Chen, B. Su, S. Liu and K. Zhao, *Adv. Funct. Mater.*, 2023, **33**, 2210765.

[4] S. Tsuda and K. Saito, *J. Environ. Radioact.*, 2017, **166**, 419.

[5] M. Moszynski, M. Kapusta, M. Mayhugh, D. Wolski and S. O. Flyckt, *IEEE Trans. Nucl. Sci.*, 1997, **44**, 1052.

[6] A. Xie, F. Maddalena, M. E. Witkowski, M. Makowski, B. Mahler, W. Drozdowski, S. V. Springham, P. Coquet, C. Dujardin, M. D. Birowosuto and C. Dang, *Chem. Mater.*, 2020, **32**, 8530.

[7] Y. Li, L. Chen, B. Liu, P. Jin, R. Gao, L. Zhou, P. Wan, Q. Xu and X. Ouyang, *J. Mater. Chem. C*, 2021, **9**, 17124.

[8] F. Zhang, Y. Zhou, Z. Chen, X. Niu, H. Wang, M. Jia, J. Xiao, X. Chen, D. Wu, X. Li, Z. Shi and C. Shan, *Laser Photonics Rev.*, 2023, **17**, 2200848.

[9] M. Zhang, X. Wang, B. Yang, J. Zhu, G. Niu, H. Wu, L. Yin, X. Du, M. Niu, Y. Ge, Q. Xie, Y. Yan and J. Tang, *Adv. Funct. Mater.*, 2021, **31**, 2007921.